energies

MDPI

*Article*

# Heat Transfer and Flow Dynamics for Natural Convection in $Fe_3O_4/H_2O$ Nanofluid

**Maryia Miadzvedzeva [1,*], Alexander S. Fedotov [2], Ilya Zur [1] and Julia Fedotova [1]**

[1] Laboratory of Physics of Perspective Materials, Research Institute for Nuclear Problems of Belarusian State University, 11 Babrujskaja Street, 220030 Minsk, Belarus; zur.ilya01@gmail.com (I.Z.); julia@hep.by (J.F.)
[2] Laboratory of High Energy Physics, Joint Institute for Nuclear Research, 4 Baldin Street, 141980 Dubna, Russia; fedotov.alehandro@gmail.com
* Correspondence: miha3272727@gmail.com; Tel.: +375-29-897-61-39

**Abstract:** $Fe_3O_4/H_2O$ nanofluid attracts many researchers' attention due to its considerable potential for practical applications. This work is focused on the study of heat transfer efficiency in $Fe_3O_4/H_2O$ nanofluids with nanoparticles (NPs) of mean diameter $d_{NPs}$ in the nanosized range (13–50 nm) at volume fractions up to 2%. The Rayleigh–Bénard problem of free convection between plane-parallel plates corresponding to Rayleigh numbers $10^3$–$10^7$ is numerically solved. It was shown that the addition of up to 2% of NPs with a diameter of 13 nm can increase the Prandtl number by up to 60% compared to pure water. A map of flow regimes is constructed, indicating the emerging convective patterns. It is demonstrated that as the volume fraction of NPs increases, the Prandtl number grows and the transition to more chaotic patterns with Rayleigh number slows down. It is observed that at a Rayleigh number of $10^4$, the heat flux through the nanofluid layer decreases by up to 25% relative to pure water. Conversely, at Ra $\approx 10^5$, the heat flux through the nanofluid layer increases by up to 18% when using a 2% volume fraction of 13 nm diameter NPs.

**Keywords:** natural convection; nanofluid; magnetite NPs; finite element method; convective patterns



Academic Editors: Tadeusz Bohdal and Marcin Kruzel

Received: 10 April 2025
Revised: 26 April 2025
Accepted: 9 May 2025
Published: 26 May 2025

**Citation:** Miadzvedzeva, M.; Fedotov, A.S.; Zur, I.; Fedotova, J. Heat Transfer and Flow Dynamics for Natural Convection in $Fe_3O_4/H_2O$ Nanofluid. *Energies* **2025**, *18*, 2767. https://doi.org/10.3390/en18112767



## 1. Introduction

In recent years, nanofluids with magnetic NPs have attracted significant scientific interest due to their unique magnetic and thermophysical properties [1–3]. These properties allow precise control of system dynamics, which is essential for applications like targeted drug delivery and theranostics [3,4]. Nanofluids—suspensions containing NPs—often exhibit enhanced thermophysical properties compared to their base solvents. Natural convection plays a significant role in heat and mass transfer in the energy industry, microelectronics, and medical applications [5–9]. For example, nanomedicine exploits convective mass transfer for the localized delivery of anticancer agents [7]. The efficiency of convective heat transfer depends on the fluid's properties, such as density, heat capacity, and thermal conductivity. According to experimental research, these properties can be improved by adding NPs [8]. There are several possible mechanisms responsible for the improvement of the thermophysical properties of a solution when NPs are added. Among them are Brownian motion, particle shape and surface charge, and thermal resistance of the phase interface. Although nanofluids have been synthesized for nearly 30 years (Choi [10] was the first to coin the term in 1995), a theoretical approach that predicts the effective properties of nanofluids taking into account the aforementioned factors has not been developed yet. Several theoretical approaches describing the rheological and thermal properties of

nanofluids, including the most commonly used Maxwell and Einstein models, have been reviewed by Kalsi et al. [11].

Commonly, NPs are synthesized from metals and semiconductors (e.g., Cu [12], Fe [13], Al [14], Si [15]), their oxides (CuO [16], $SiO_2$ [16], $Fe_2O_3$ [17], $Fe_3O_4$ [18], $Al_2O_3$ [19]) or carbonaceous materials (carbon nanotubes [16,20], graphene [21,22]), and are suspended in a base fluid such as water [20], oil [22], ethylene glycol (EG) [17], kerosene [23] or another. Metal oxide NPs are of exceptional interest because they are non-toxic, widely available and show favorable physical and chemical properties such as high chemical stability and sufficiently high saturation magnetization to be applied as a theranostic platform [24].

One of the challenges in the synthesis of nanofluids is the aggregation of particles due to their surface charge, which causes sedimentation instability that is normally neutralized by Brownian motion. Aggregation leads to an increase in the viscosity of the suspension [25], which is undesirable for thermophysical applications since it suppresses convection. In this paper, pure water is considered as the base medium, and $Fe_3O_4$ (magnetite) is considered as a dispersed phase. The aggregation of suspended $Fe_3O_4$ NPs can be moderately reduced by applying additional polymer coatings. Such nanosized crystallites are in demand in recent investigations because of their superparamagnetic and biocompatible properties [26], colloidal stability, and controlled size [27]. Magnetite NPs within 10–100 nm coated with surfactants easily penetrate the biological media [27]. In biomedical applications, they have been used to induce heating for hyperthermia treatments and the remote control of convection-enhanced targeted drug delivery [4,28]. Thus, $Fe_3O_4$ stands out as a promising material due to its high magnetic and distinctive behavior in aqueous solutions.

While the properties of buoyancy-driven convection in bare fluids are well-studied, free convection in nanofluids receives attention as well. Works on the topic of free convection and heat transfer in water-based nanofluids describe the results for a wide spectrum of NPs (diamond [29], Cu [29], CuO [30], $Al_2O_3$ [30,31], etc.), as well as for magnetite ones in the presence of an external magnetic field and within cavities with complex geometry [32,33]. Besides traditional mesh-based techniques, significant progress has been achieved by using less traditional approaches. For example, Feng and Wang [34] investigated $Fe_3O_4/H_2O$ nanofluid–porous media with a nonorthogonal Lattice Boltzmann method (LBM) and found the possibility of controlling Nusselt (Nu) and Sherwood (Sh) numbers by 50–200% by varying the buoyancy ratio from $-1.3$ to 1.3, Lewis number from 1 to 5 and porosity from 0.2 to 0.8. Weng et al. [35] found that an EG/iron nanofluid increase in Rayleigh number from $10^3$ to $10^5$ leads to a Nu increase of 44%, while an increase from $10^5$ to $10^6$ leads to a Nu increase of 118%. L. Li et al. [36,37] implemented coupled Lattice Boltzmann-Large Eddy Simulation-Discrete element method and revealed the possibility of ultrasound exploitation for the local suppression of NP agglomeration in critical flow regions, and proved it experimentally [38,39]. Chen et al. [40] in an extensive review showed that molecular dynamics provide insights into microscopic interactions between NPs and base fluids, deepening the understanding of heat properties and aggregation parameters, though accurate determination of force potentials remains challenging. Still, as Alsabery et al. [41] remarked, 81% of modern studies rely on single-phase models with effective properties, providing new results. In work by Khanafer et al. [42], it was shown that suspended Cu NPs intensify heat transfer, resulting in an increase of the Nusselt number by up to 25% compared to pure water. In theoretical work [43], natural convection of nanofluids in different enclosures was extensively studied for Rayleigh numbers (Ra) smaller than $2 \times 10^4$, and an increase of Nu was found for all types of NPs under consideration (Ag, Cu, CuO, $Al_2O_3$, and $TiO_2$). In the experimental study [44], no changes in effective heat transfer performance were observed for $Al_2O_3/H_2O$ and $Cu/(CH_2OH)_2$ nanofluids. The increase of about 35% in Nu was reported for MWCNT/water nanofluid [45].

Still, in theoretical work [46], $Fe_3O_4/H_2O$ nanofluid showed enhancement of less than 1% in the Nusselt number with a volume fraction of NPs in the range of Rayleigh numbers $10^4$–$10^6$. In a recent experimental study of $Fe_3O_4/H_2O$ nanofluid by Kamran and Qayoum [47], it was shown that the Nusselt number grows with volume fraction up to 2% in comparison to a base fluid for $Ra > 2 \times 10^7$. Kamran and Qayoum [47] examined a cubic experimental cell where finite size and boundary effects significantly affect the dynamics of heat transfer. In fact, the shape or aspect ratio of the heat exchanger can noticeably influence the convective performance [48]. Pazarlioglu and Tekir [46] investigated a simplified two-dimensional model that includes a single convection roll within a periodic domain. Two-dimensional models cannot resolve self-organized convective texture patterns, a crucial aspect of high-intensity convection [49,50]. Therefore, a study that considers a three-dimensional problem with minimized influence of boundaries may provide useful insight into a convection phenomenon for $Fe_3O_4/H_2O$ nanofluid.

It seems that additional studies are required, as the systematic data for $Fe_3O_4/H_2O$ remain sparse. Published studies focus on (i) small Rayleigh numbers ($Ra < 2 \times 10^4$) [42] or (ii) cubic cavities with pronounced wall effects [47]. Thus, the range of $Ra \approx 10^3$–$10^7$, which is particularly interesting from a physical perspective due to the emergence of convective textures and the large aspect ratio of the domain that minimizes boundary effects, is neglected. No three-dimensional simulation has been carried out yet to investigate the full convective pattern sequence linked to heat-flux changes in $Fe_3O_4/H_2O$ nanofluids.

The present work therefore fills two gaps: (i) it provides the 3D, large-aspect-ratio Rayleigh–Bénard analysis of $Fe_3O_4/H_2O$ across $10^3 \leq Ra \leq 10^7$, and (ii) it establishes how nanoparticle diameter (13 nm vs. 30–50 nm) and volume fraction ($\varphi \leq 2\%$) jointly control convective textures and global heat transfer efficiency. These insights supply design rules for magnetite-based coolant layers in electronics and biomedical devices.

Thus, the aim of this paper is to study convection dynamics in $Fe_3O_4/H_2O$ nanofluid. We perform numerical simulations of the three-dimensional Rayleigh–Bénard problem in $Fe_3O_4/H_2O$ nanofluid using a fundamental heat exchanger geometry—a parallelepiped with a height significantly less than its length and width to reduce finite-size boundary effects. By means of a developed finite element model of 3D Rayleigh–Bénard problem, we are able to compute the temperature and velocity distributions in the domain, as well as to estimate the effect of $Fe_3O_4$ NPs volume fraction $\varphi$ in the range of 0–2% on the Prandtl number (Pr) and driving temperature gradient in the range of Rayleigh numbers ranging between $10^3$–$10^7$.

## 2. Materials and Methods

The convective movement of an incompressible flow is described by a system of hydrodynamic equations under the Boussinesq approximation. This system includes the Navier–Stokes equations, the heat transfer equation and the continuity equation. The density is assumed to be a linear function of temperature and independent of pressure due to the incompressibility of the flow. Since we consider volume fractions φ less than 2%, the influence of NPs is accounted for through the effective properties of the nanofluid: viscosity, thermal conductivity, density and heat capacity. With regard to the relevant physical quantities, we can write the system in a dimensionless form. A particular feature of convective problems is the absence of a characteristic velocity scale, as the flow is driven solely by the applied temperature gradient. Therefore, a characteristic length $L$ is typically chosen as the unit of distance, and the characteristic temperature difference $\Delta T$ serves as the unit of temperature. In this context, the velocity scale is introduced as $\frac{\chi}{L}$, the time scale

as $\frac{L^2}{\nu}$ and the pressure scale as $\frac{\rho_0 \nu^2}{L^2}$, where $\chi$ is the thermal diffusivity, $\nu$ is the kinematic viscosity coefficient and $\rho_0$ is fluid density at the reference temperature $T_0$. Hence,

$$\begin{cases} \frac{\partial \vec{v}}{\partial t} + (\vec{v} \cdot \nabla)\vec{v} = -\nabla P + \nabla^2 \vec{v} + \mathrm{Ra}(\varphi) T \vec{e}_z, \\ \mathrm{Pr}(\varphi)\frac{\partial T}{\partial t} + (\vec{v} \cdot \nabla)T = \nabla^2 T, \\ \mathrm{div}\ \vec{v} = 0, \\ \rho = \rho_0(\varphi)(1 - \beta(T - T_0)), \end{cases} \tag{1}$$

$$\mathrm{Ra} = \frac{g\beta\Delta T h^3}{v(\varphi)\chi(\varphi)}, \tag{2}$$

$$\mathrm{Pr} = \frac{v(\varphi)}{\chi(\varphi)}. \tag{3}$$

where $\vec{v}$ is the velocity, $P$ is the pressure, $\rho$ is the fluid density, $g = 9.8067\ \mathrm{m/s^2}$ is the gravity constant, $\beta$ is the coefficient of thermal expansion, $T$ is the local temperature, $\vec{e}_z$ is the unit vector aligned with the direction of gravity, $\Delta T = T_{bottom} - T_{top}$ is the difference between the lower and upper boundaries' temperatures.

Although COMSOL Multiphysics 6.2 operates as a dimensioned code [51], we present the Navier–Stokes and energy equations in non-dimensional form (1), where the Rayleigh and Prandtl numbers emerge naturally as the only free parameters. The Rayleigh number in (2) represents the ratio of buoyancy forces to viscous forces. The Prandtl number in (3) characterizes the similarity between the velocity and temperature fields. In other words, it compares the thicknesses of the thermal and velocity boundary layers [52] and controls the relative rates of heat and momentum transport. For Pr < 1, thermal diffusion prevails over momentum diffusion, yielding broader thermal boundary layers and smoother temperature fields, whereas for Pr > 1, the thinner thermal layers and stronger momentum diffusion promote sharper, finer convective structures. Furthermore, the Prandtl number is independent of the geometry of the computational domain and is determined solely by the physical properties of the fluid.

The free convection problem was solved numerically in COMSOL Multiphysics using the finite element method. The computational domain was a parallelepiped with a height of $h = 0.1$ m and length and width $L = 3$ m each, resulting in an aspect ratio $\frac{h}{L} = 0.03$. Such geometry, combined with periodic boundary conditions, limits the influence of side walls on flow dynamics.

A non-uniform mesh was generated, including near-wall regions with layers of rectangular elements that stretch as the layer approaches a solid boundary (Figure 1). The domain was divided into $1.8 \times 10^5$ elements, including $1.3 \times 10^4$ elements for boundary layers.

The mesh resolution must be chosen so that the smallest length scales of the flow are resolved [53]. Accordingly, the ratio of maximum mesh element width $\Delta_{max}$ to the Kolmogorov length scale $\eta$

$$\eta = \frac{h \cdot \mathrm{Pr}^{1/2}}{(Ra \cdot (Nu - 1))^{1/4}} \tag{4}$$

and the Batchelor length scale $\eta_B$

$$\eta_B = \eta \cdot \mathrm{Pr}^{-1/2} \tag{5}$$

should not exceed unity for an adequate numerical solution [54]:

$$\frac{\Delta_{\max}}{\eta} < 1, \quad \frac{\Delta_{\max}}{\eta_B} < 1. \tag{6}$$

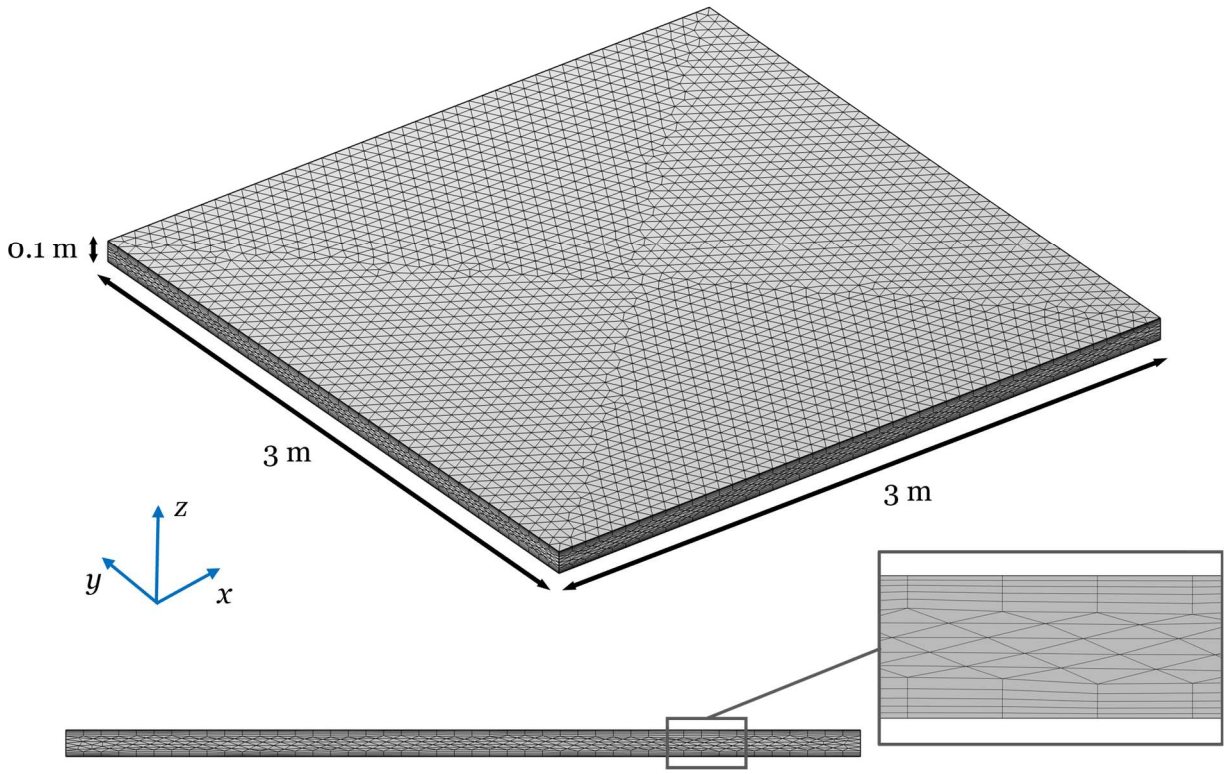


**Figure 1.** Mesh of the computational domain.

In this simulation, the maximum mesh element width was approximately $\Delta_{max} \approx 0.005$ m, so condition (6) was satisfied with at least 90% of the energy in the Kolmogorov spectrum for solutions with Ra up to $10^7$.

To solve the incompressible Navier–Stokes equations, COMSOL Multiphysics applies an incremental pressure-correction scheme [55], where the pressure field is iteratively updated to enforce the divergence-free condition for velocity. Firstly, the velocity components $\vec{v}^{n+1}$ are predicted from the discretized Navier–Stokes equation, with the time derivatives approximated by the second-order backward differentiation formula (BDF2):

$$\frac{3\vec{v}^{n+1} - 4\vec{v}_c^{n} + \vec{v}_c^{n-1}}{2\tau} + \vec{v}_c^{n} \cdot \nabla \vec{v}^{n+1} = -\frac{1}{\rho}\nabla p_c^n + \nabla\left(\nu\left(\nabla \vec{v}^{n+1} + \left(\nabla \vec{v}^{n+1}\right)^T\right)\right) + \vec{g}. \quad (7)$$

Here, $\tau$ is the timestep, the subscript '$n$' refers to the timestep index and the subscript '$c$' denotes the corrected variable value. Subsequently, Poisson's equation is solved to adjust the pressure:

$$\tau\,\Delta\left(p_c^{n+1} - p_c^n\right) = -\nabla \cdot \rho\,\vec{v}^{n+1}. \quad (8)$$

Finally, the velocity field is corrected based on the updated pressure distribution:

$$\vec{v}_c^{n+1} = \vec{v}^{n+1} - \frac{\tau}{\rho}\nabla\left(p_c^{n+1} - p_c^n\right). \quad (9)$$

Velocity, pressure and temperature are discretized in space by linear elements "P1 + P1", which gives an error no worse than $O(h)$ and guarantees the absence of solution oscillations inside elements.

To prevent any external influence and focus on internal instability, the fluid was initially at rest. For the acceleration of the convergence, the lower half of the domain was pre-heated to $T_0 + \Delta T$. The initial conditions were set as follows:

$$\begin{cases} \vec{v}\Big|_{t=0} = 0,\ (x,y,z) \in D, \\ p|_{t=0} = \rho g z,\ (x,y,z) \in D, \\ T\Big|_{t=0, z \geq \frac{h}{2}} = T_{top} = T_0,\ (x,y,z) \in D, \\ T\Big|_{t=0, z < \frac{h}{2}} = T_{bottom} = T_0 + \Delta T,\ (x,y,z) \in D \end{cases} \tag{10}$$

where $D$ is the computational domain volume, $h$ is the height of the domain, $T_{top}$ and $T_{bottom}$ are the temperatures of the upper and lower boundaries, respectively ($T_0$ = 293.15 K, $T_{bottom} > T_{top}$). The initial pressure gradient caused by hydrostatics ensures mechanical equilibrium without generating the flow.

The boundary conditions were the following:

$$\begin{cases} \vec{v}\Big|_{z=0,\ z=h} = \vec{0},\ (x,y) \in, \\ \vec{v} \cdot \vec{n}\Big|_{x=0,\ x=L} = 0,\ (y,z) \in, \\ \vec{v} \cdot \vec{n}\Big|_{y=0,\ y=L} = 0,\ (x,z) \in, \\ \left(-pI + \nu\left(\nabla \cdot \vec{v} + \left(\nabla \cdot \vec{v}\right)^T\right)\right) \cdot \vec{n}\Big|_{x=0,\ x=L} = 0,\ (y,z) \in, \\ \left(-pI + \nu\left(\nabla \cdot \vec{v} + \left(\nabla \cdot \vec{v}\right)^T\right)\right) \cdot \vec{n}\Big|_{y=0,\ y=L} = 0,\ (x,z) \in, \\ T|_{z=0} = T_{top},\ (x,y) \in, \\ T|_{z=h} = T_{bottom},\ (x,y) \in, \\ \vec{q} \cdot \vec{n}\Big|_{x=0,\ x=L} = 0,\ (y,z) \in, \\ \vec{q} \cdot \vec{n}\Big|_{y=0,\ y=L} = 0,\ (x,z) \in \end{cases} \tag{11}$$

where $\Gamma$ is the boundary of the domain, $L$ is the side length of the upper and lower plates, $\vec{n}$ is the local normal unit vector to the side boundary, $I$ is the identity matrix, and $\vec{q}$ is the heat flux (Figure 2).

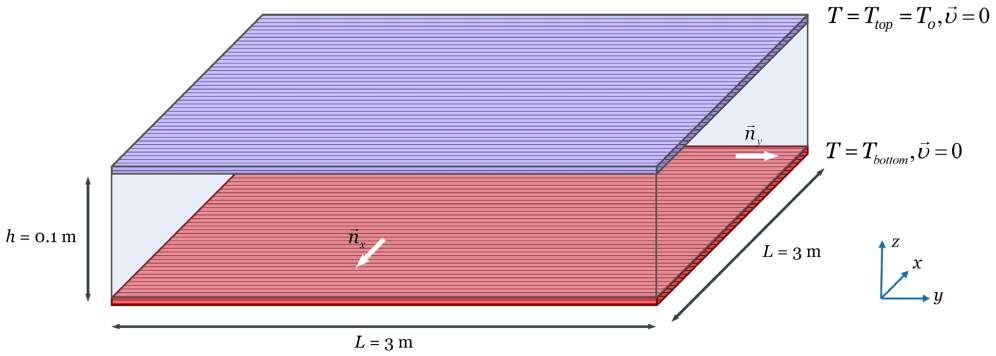


**Figure 2.** Boundary conditions scheme.

Thence, the upper and lower boundaries were considered as solid walls keeping a constant temperature difference $\Delta T$. The heat flux conditions on the side boundaries of the domain were set adiabatic and symmetrical. By imposing such conditions on the sidewalls, we eliminate the influence of finite physical boundaries on the pattern [56]. Compared

to periodic conditions, this approach prevents pattern drifting through the boundaries, making the pattern easier to track.

To account for the influence of NPs on the pure water, we evaluated effective thermophysical properties of nanofluids such as thermal conductivity $\kappa$ and dynamic viscosity $\mu$ from [47,57]. Sundar et al. [57] provide data for nanofluid containing NPs with $d_{NPs}$ = 13 nm and Pr $\in$ (5.4; 9.0) over the volume fraction range $\varphi$ = 0–2%. The authors synthesized magnetite NPs and estimated their average core diameter using the Scherrer equation applied to the XRD data [57]. Kamran et al. [47] provide data for nanofluid containing NPs with $d_{NPs}$ = 30–50 nm and Pr $\in$ (6.9; 7.6) over the volume fraction range $\varphi$ = 0–0.6%. We considered both cases separately in this study.

Density and specific heat capacity for each dataset were evaluated using empirical relations proposed by Pak and Cho [58], with respect to pure water parameters reported in the works above:

$$\rho_{nf} = \varphi\rho_{np} + (1-\varphi)\rho_{bf}, \tag{12}$$

$$C_{p,nf} = \varphi C_{p,np} + (1-\varphi)C_{p,bf}, \tag{13}$$

where the subscripts '*nf*', '*np*' and '*bf*' denote nanofluid, NP and base fluid, respectively. The obtained data are presented in Tables 1 and 2.

**Table 1.** Thermophysical properties of $Fe_3O_4/H_2O$ nanofluid containing NPs with $d_{NPs}$ = 13 nm at $T_0$ = 293.15 K according to Sundar et al. [57].

| Volume Fraction $\varphi$, % | Density $\rho$, kg/m$^3$ | Thermal Conductivity $\kappa$, W/m·K | Dynamic Viscosity $\mu$, mPa·s | Kinematic Viscosity $\nu \times 10^{-6}$, m$^2$/s | Specific Heat Capacity $C_p$, J/kg·K | Thermal Diffusivity $\chi \times 10^{-7}$, m$^2$/s |
|---|---|---|---|---|---|---|
| 0 | 999 | 0.602 | 0.79 | 0.79 | 4182 | 1.44 |
| 0.2 | 1008 | 0.652 | 0.84 | 0.83 | 4174 | 1.55 |
| 0.6 | 1027 | 0.690 | 1.01 | 0.98 | 4160 | 1.61 |
| 1 | 1046 | 0.730 | 1.44 | 1.38 | 4146 | 1.68 |
| 2 | 1095 | 0.753 | 1.65 | 1.51 | 4111 | 1.67 |

**Table 2.** Thermophysical properties of $Fe_3O_4/H_2O$ nanofluid containing NPs with $d_{NPs}$ = 30–50 nm at $T_0$ = 293.15 K according to Kamran et al. [47].

| Volume Fraction $\varphi$, % | Density $\rho$, kg/m$^3$ | Thermal Conductivity $\kappa$, W/m·K | Dynamic Viscosity $\mu$, mPa·s | Kinematic Viscosity $\nu \times 10^{-6}$, m$^2$/s | Specific Heat Capacity $C_p$, J/kg·K | Thermal Diffusivity $\chi \times 10^{-7}$, m$^2$/s |
|---|---|---|---|---|---|---|
| 0 | 999 | 0.607 | 1.00 | 1.00 | 4182 | 1.45 |
| 0.2 | 1008 | 0.643 | 1.16 | 1.15 | 4174 | 1.53 |
| 0.6 | 1027 | 0.662 | 1.21 | 1.18 | 4160 | 1.55 |

To obtain solutions in the range of Ra $\in$ ($10^3$; $10^7$), the corresponding modeling temperature range was determined: $T \in$ (293.15; 294.15) K and $\Delta T \in$ (0.0005; 1.0000) K. Although $\Delta T$ of up to 1 K may appear small in typical industrial or biomedical applications, it may be used in certain microfluidic devices or temperature-sensitive diagnostics in biomedical research, where even minor fluctuations can affect fluid flow or biological activity.

The usual approach to evaluating heat transfer efficiency in a fluid-filled region is to estimate the integral Nusselt number, which indicates how many times the heat flux is enhanced by convection compared to pure diffusion alone [59]. However, in our study, the thermal conductivity of nanofluids varies with $\varphi$ (see Tables 1 and 2), causing the diffusion contribution to grow slightly faster than the convective contribution. This may give a misleading impression of heat transfer suppression due to a decrease in Nu, whereas in reality, the total heat transfer rate benefits from both convection and diffusion. Therefore, instead of analyzing Nu directly, we focus on the absolute heat flux and its changes.

Before undertaking the actual numerical calculation, it is mandatory to provide a grid independence study to ensure that the computed quantities are not corrupted by the mesh resolution. Mesh refinement reduces discretization errors and enhances the accuracy of

the solution. However, rounding errors also increase as the number of discrete points increases [37]. Figure 3 depicts the variation of the Nusselt number for the selected nanofluid as a function of the number of mesh elements. The chosen case of about $1.8 \times 10^5$ elements represents a good compromise between solution quality and computational cost: with further refinement, the model yields a stable prediction of the Nusselt number.

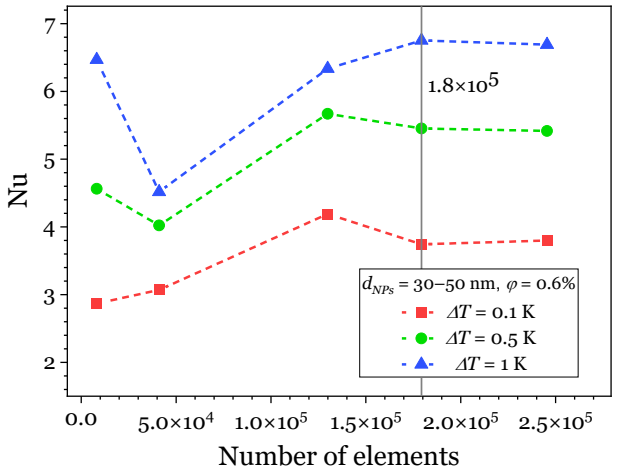


**Figure 3.** Grid independence verification: Nusselt number dependence on the number of elements for a nanofluid with $d_{NPs}$ = 30–50 nm and $\varphi$ = 0.6%.

## 3. Results and Discussion

### *3.1. Prandtl Number*

The Prandtl number of nanofluids and pure water at $\varphi$ = 0%, evaluated based on data from Tables 1 and 2, is shown in Figure 4. The dependence of Pr on $\varphi$ for $d_{NPs}$ = 13 nm particles can be divided into two sections, before and after a step at $\varphi \approx 1\%$. The Prandtl number increases from approximately 5.4 at $\varphi$ = 0–0.2% to 8.2 at $\varphi$ = 1%. After $\varphi$ = 1%, the thermal diffusivity becomes less susceptible to further increases in volume fraction of NPs (see Table 1), leading to a weaker Pr($\varphi$) dependence. For nanofluids containing NPs with $d_{NPs}$ = 30–50 nm, we observe a similar trend: as the volume fraction increases from 0 to 0.6%, the rate of change in the Pr declines.

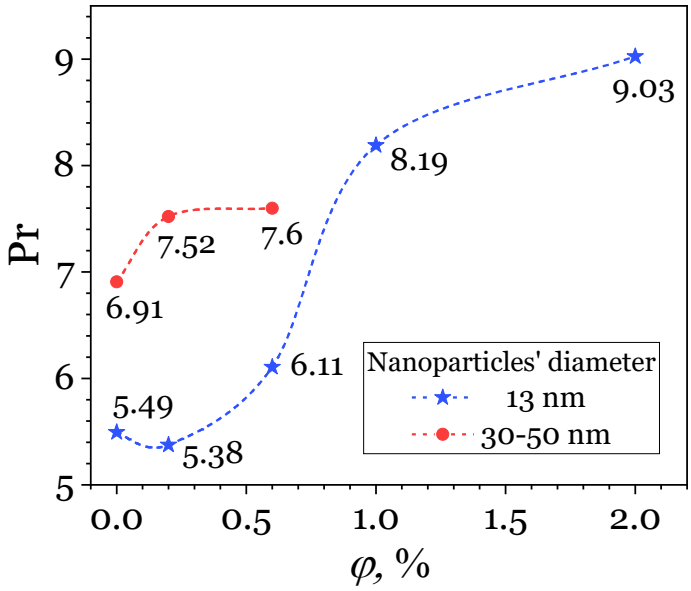


**Figure 4.** Dependence of Pr on the volume fraction $\varphi$ of $Fe_3O_4$ NPs.

Overall, as can be seen from Figure 4, Pr increases with NPs volume fraction $\varphi$, indicating a growing role of viscous damping over heat diffusion [60].

### *3.2. Convection Dynamics Analysis*

We computed the spatial distributions of temperature and velocity for a temperature difference between the hot and the cold boundary $\Delta T$ up to 1 K, corresponding to Ra $\in (10^3; 10^7)$. Computations were performed for $Fe_3O_4$ volume fractions $\varphi$ up to 2% using density, thermal conductivity and viscosity from Sundar et al. [57] (for NPs with $d_{NPs}$ = 13 nm), and for $\varphi$ up to 0.6% using similar data from Kamran et al. [47] (for NPs with $d_{NPs}$ = 30–50 nm). In order to analyze the resulting convective pattern, distributions of physical quantities were plotted on a slice at half the height of the computational domain (see Figure 5).

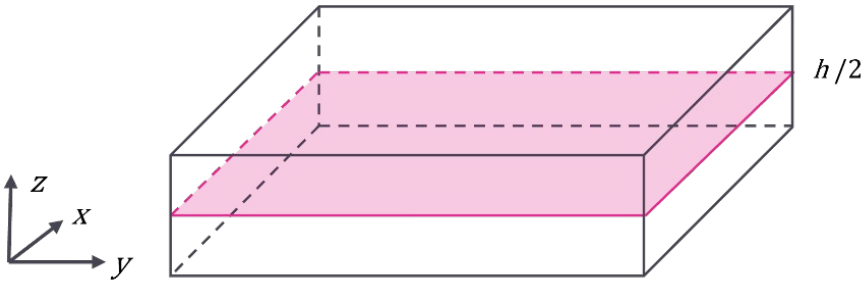


**Figure 5.** Placement of the *xy*-cut plane at a height of $h/2$.

Figures 6 and 7 show the normalized distributions of temperature and velocity magnitude for various temperature differences $\Delta T$ and NPs volume fractions $\varphi$. There are five different types of convective patterns observed. While Figure 6 provides information on temperature, we recommend referring to Figure 7, as the velocity magnitude highlights the boundaries of the convective cells more clearly.

At $\varphi$ = 1% and 2% with $\Delta T = 5 \times 10^{-4}$ K, Ra is very close to the critical value, leading to a uniform pattern with no distinct structures. In pure water at $\Delta T = 5 \times 10^{-4}$ K, and in all nanofluids at $\Delta T = 1 \times 10^{-3}$ K, we observe a pattern with numerous centers overlaid by a labyrinth pattern, classified according to [61]. As $\Delta T$ increases from $5 \times 10^{-3}$ K to $1 \times 10^{-2}$ K, the labyrinth pattern shows an increasing number of so-called 'spiral defects' [50,62]. At $\Delta T$ = 0.05 K, and $\Delta T$ = 0.1 K for $\varphi$ = 1% and 2%, bigger convective cells are formed, with a different (super)-scale [49,63]. For even larger $\Delta T$, up to a maximum of 1 K, we observe a transition to a fully turbulent regime.

Figure 8 presents spatial distributions of temperature and velocity magnitude for nanofluids containing NPs with $d_{NPs}$ = 30–50 nm. In general, we observe the same evolution of patterns with $\Delta T$ as seen for the case of $d_{NPs}$ = 13 nm particles: a uniform pattern at lower Ra, then a labyrinth-like wavy pattern, followed by a spiral defect pattern, the formation of supercells, and finally, a transition to turbulent chaos at higher $\Delta T$.

Generally, both types of nanofluids containing NPs with $d_{NPs}$ = 13 nm and $d_{NPs}$ = 30–50 nm show a similar trend: the increase of $\varphi$ suppresses the convection mechanism, making the pattern less chaotic.

Using the data presented in Figures 6–8, we constructed flow regime maps shown in Figure 9. The points represent the computed data, while the surrounding regions are the corresponding Voronoi polygons. It can be seen that at Ra $\approx 3 \times 10^3$, the pattern becomes uniform for $\varphi \geq 0.2\%$ for nanofluid with $d_{NPs}$ = 30–50 nm, whereas for $d_{NPs}$ = 13 nm, the uniform pattern appears at $\varphi \geq 1\%$.

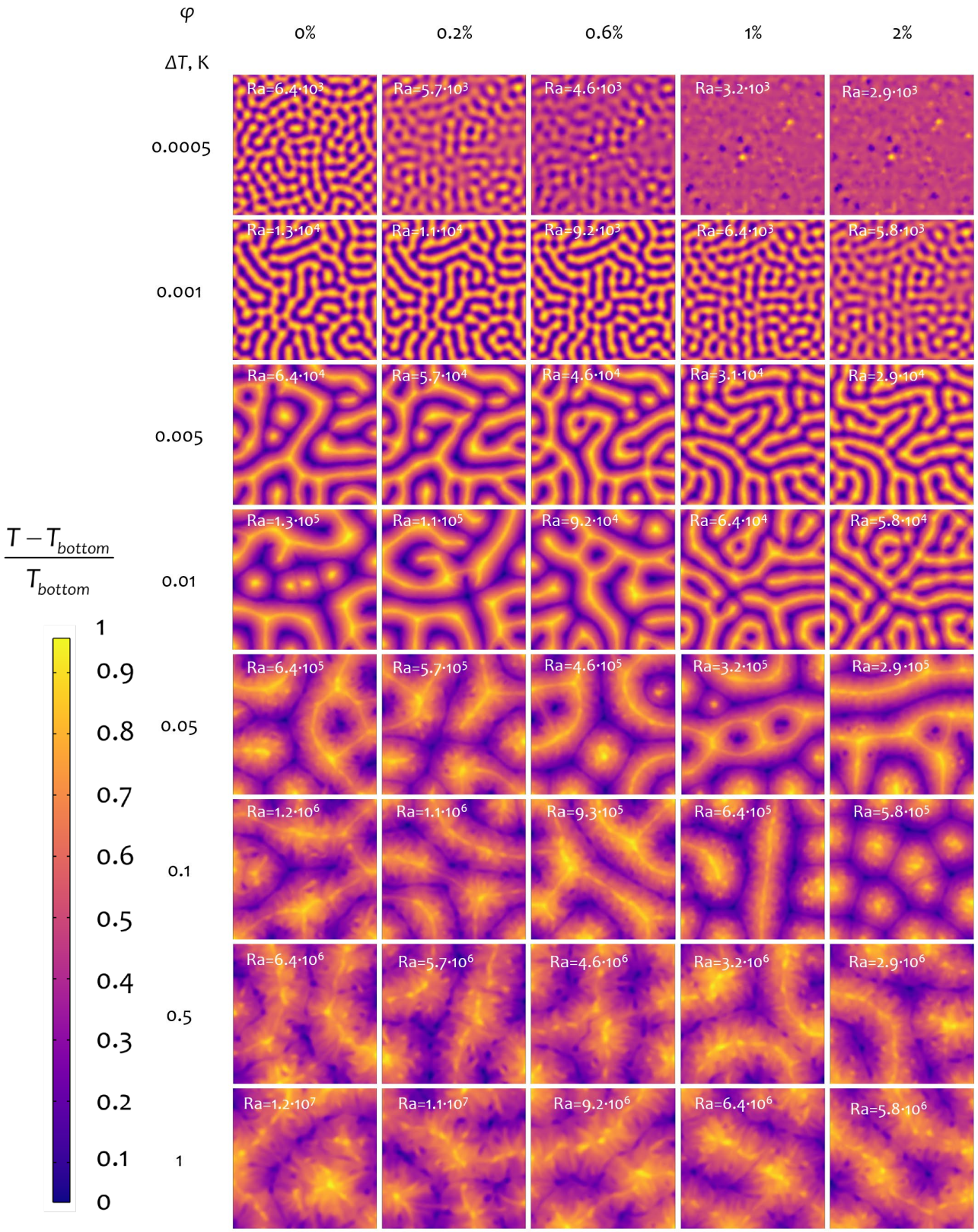


**Figure 6.** Spatial distributions of normalized temperature in the *xy*-cut plane at a height $h/2$ for nanofluid containing NPs with $d_{NPs}$ = 13 nm for different NPs volume fractions $\varphi$ and temperature differences $\Delta T$.

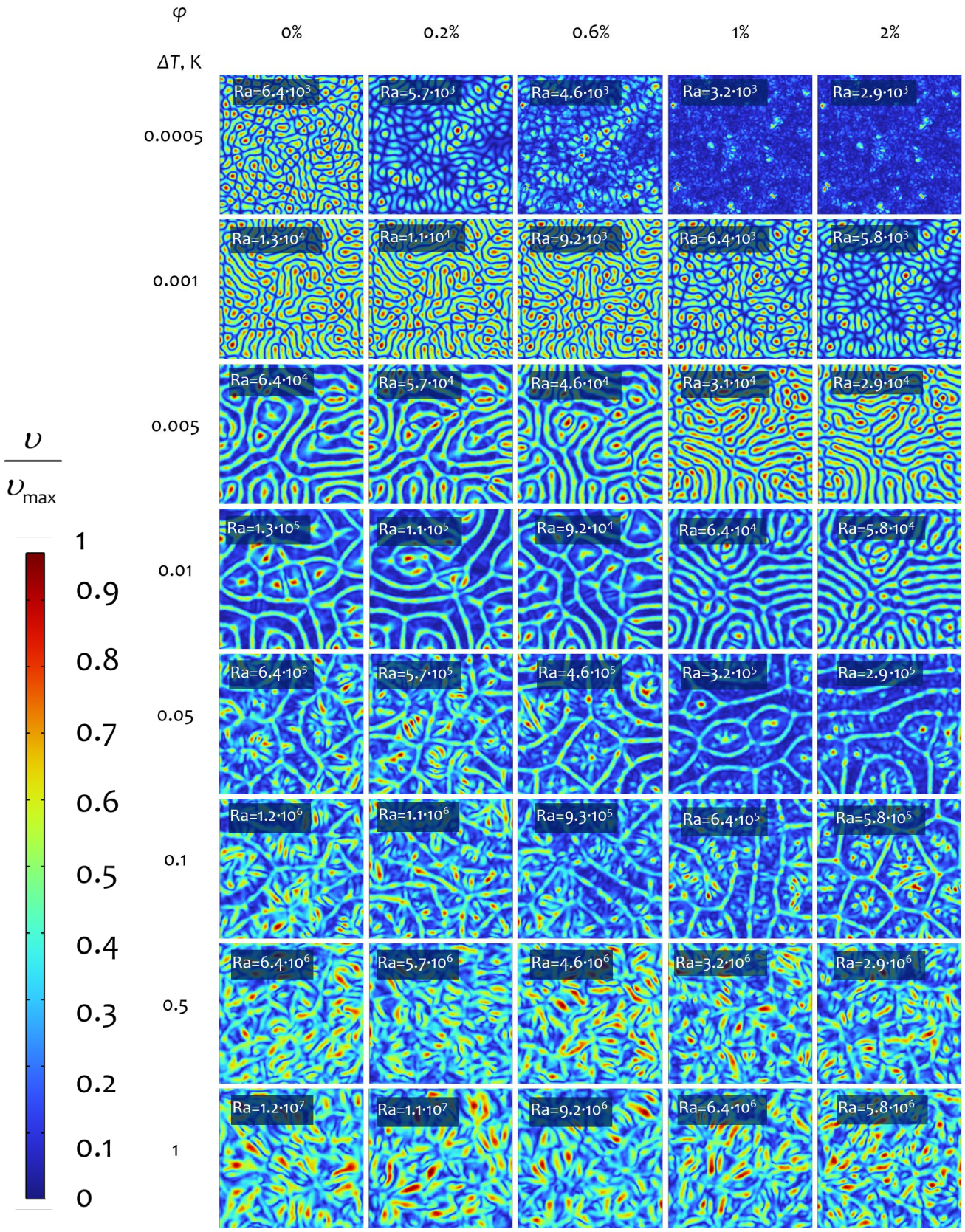


**Figure 7.** Spatial distributions of normalized velocity magnitude in the $xy$-cut plane at a height $h/2$ for nanofluid containing NPs with $d_{NPs}$ = 13 nm for different NPs volume fractions $\varphi$ and temperature differences $\Delta T$.

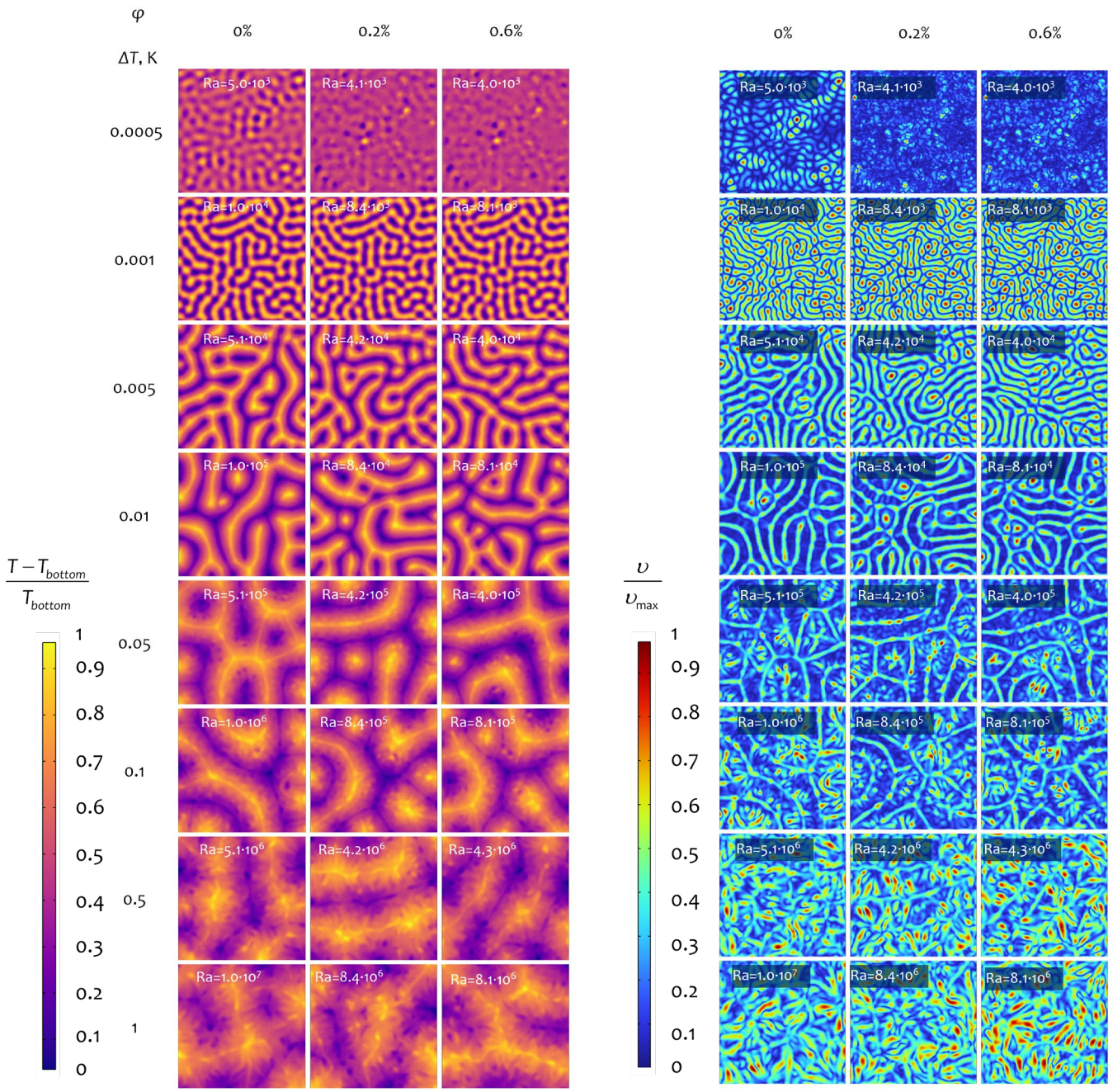


**Figure 8.** Spatial distributions of (**a**) normalized temperature and (**b**) normalized velocity magnitude in the *xy*-cut plane at a height $h/2$ for nanofluid containing NPs with $d_{NPs}$ = 30–50 nm for different NPs volume fractions $\varphi$ and temperature differences $\Delta T$.

For φ up to 0.6%, the transition from a labyrinth pattern to a spiral defect one occurs at Ra ≈ $5 \cdot 10^4$ in the nanofluid with $d_{NPs}$ = 30–50 nm. For the case of $d_{NPs}$ = 13 nm at the same fractions, the transition occurs at Ra ≥ $1 \cdot 10^5$. This behavior is more akin to the nanofluid with $d_{NPs}$ = 13 nm at $\varphi \geq 1\%$. Such a difference in pattern dynamics is consistent with the Prandtl number trends in Figure 4: Pr for nanofluids with $d_{NPs}$ = 30–50 nm at volume fractions up to 0.6% is close to nanofluids with $d_{NPs}$ = 13 nm at volume fractions of 1−2%.

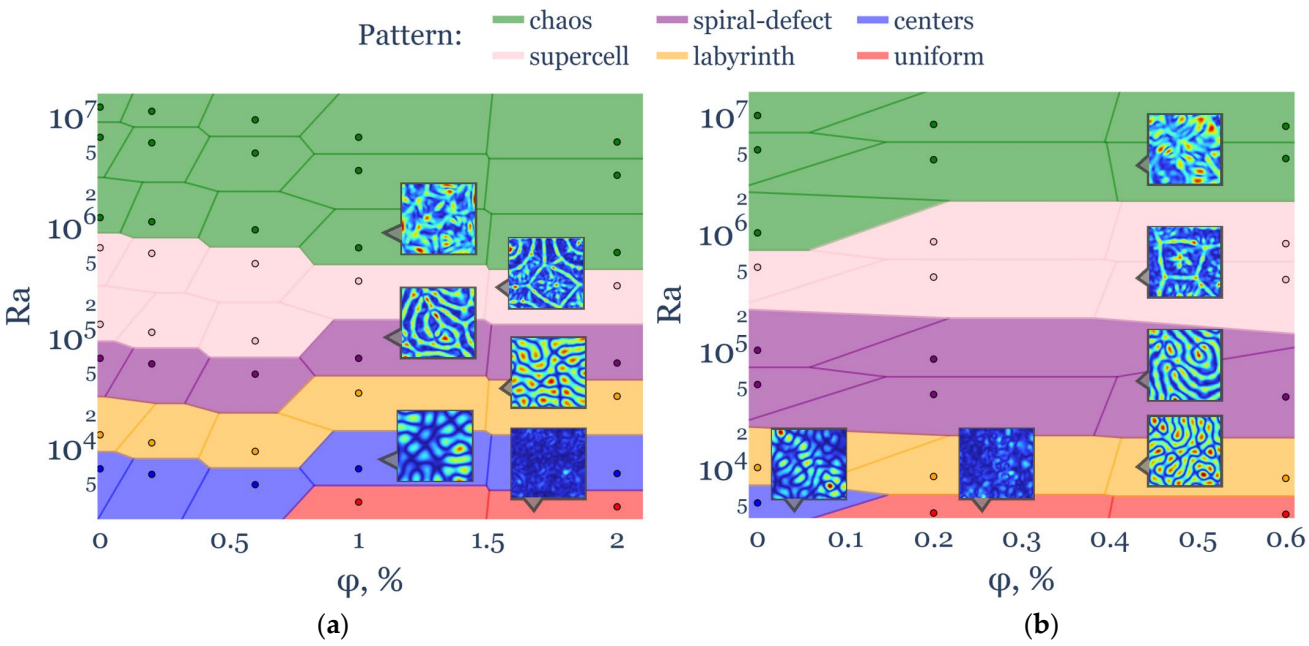


**Figure 9.** Free convection flow regime maps in Ra-$\varphi$ coordinates for input material properties for nanofluids containing NPs with $d_{NPs}$ = 13 nm (**a**) and $d_{NPs}$ = 30–50 nm (**b**).

The transition to turbulent convection at Ra $\geq 1 \cdot 10^6$ is manifested in the enlargement of the roll pattern and distortion of rolls' outlines by velocity pulsations. In such a case, one speaks of highly diffusive temperature fields that are in conjunction with an inertia-dominated fluid turbulence [49].

The influence of the Prandtl number on flow organization can, in this context, be interpreted through the lens of volume fraction effects, since, as illustrated in Figure 4, an increase in NP volume fraction is accompanied by a rise in Prandtl number. A parallel argument applies to viscosity, given its direct proportionality to Pr in Equation (3). Accordingly, in more viscous media, under fixed $\Delta T$, the flow exhibits reduced dynamism, while the pattern assumes a finer and more distinct structure. Notably, the evolution of convective patterns in the studied nanofluids unfolds via different scenarios. In the nanofluid with $d_{NPs}$ = 13 nm, at lower fractions $\varphi$ = 0–0.6%, the onset of a new pattern regime occurs at lower thresholds as the Rayleigh number increases compared to higher fractions $\varphi$ = 1–2%. This correlates with the sharp increase in the Prandtl number at $\varphi \gtrsim 1\%$. In contrast, for nanofluids containing NPs of $d_{NPs}$ = 30–50 nm, the transition emerges nearly synchronously across all examined volume fractions as Ra increases.

Figure 10 illustrates the evolving flow structures in the normalized temperature field, marked from (**a**) to (**f**) in the order of their emergence with Ra. Since the heat exchanger geometry represents a thin layer, a scaling along the *z*-axis is applied to all 3D distributions to enhance the visualization. As the bottom plate heats up, multiple structures elongate vertically, forming column-like plumes (appearing as labyrinths in the cut-plane view), and then gradually merge into a roll pattern.

### *3.3. Heat Transfer Efficiency*

Figure 11a shows the dependence of the mean heat flux through the boundary $<q_b>$ on Ra. For Ra $\geq 10^5$, nanofluids with the highest NPs volume fractions exhibit an increased heat flux in comparison to pure water. Figure 11b shows that the difference in heat flux between a nanofluid containing NPs with $d_{NPs}$ = 30–50 nm and pure water is less than that of a nanofluid containing NPs with $d_{NPs}$ = 13 nm.

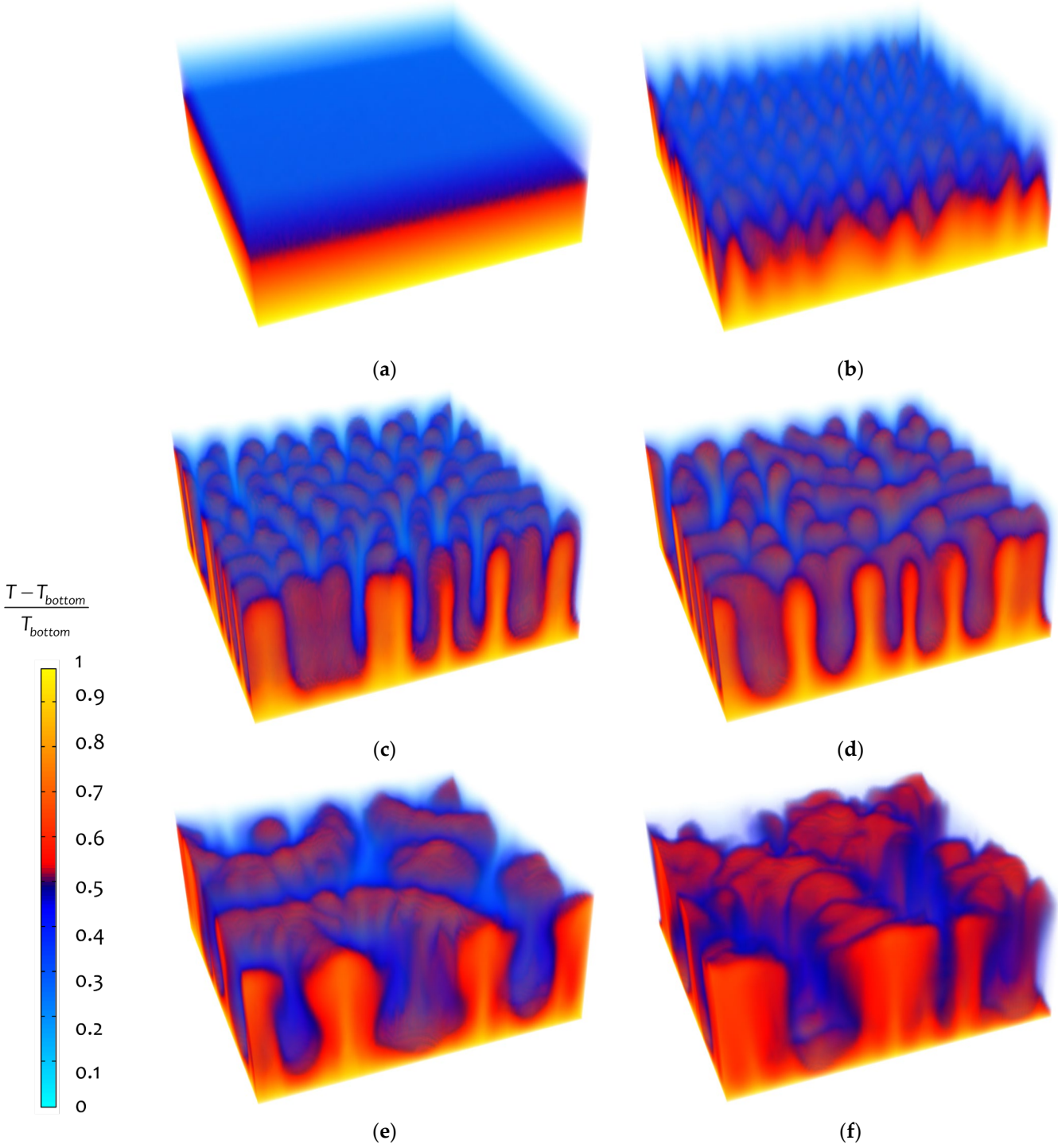


**Figure 10.** Volumetric distributions of normalized temperature for different convective patterns: (**a**) uniform, (**b**) centers, (**c**) spiral defect, (**d**) labyrinth, (**e**) supercell, (**f**) chaos.

In Figure 11b, the relative change in heat flux $<q_b>$ compared to pure water $<q_{0\%}>$ is given. At $\Delta T$ = 0.001 K, there is a minimum in the relative heat flux for nanofluids with higher Prandtl numbers: namely, for nanofluids with $d_{NPs}$ = 13 nm at $\varphi \geq 1\%$ and for all nanofluids with $d_{NPs}$ = 30–50 nm. As shown in Figure 11b, about 18% of the heat transfer efficiency may be lost at the corresponding Ra $\approx 10^4$ compared to pure water. Subsequently, at $\Delta T$ = 0.05 K (Ra $\approx 10^5$), heat transfer in nanofluid becomes more efficient than water for all nanofluids, with the strongest gain appearing for $d_{NPs}$ = 13 nm at $\varphi$ = 1% and 2%. However, with a further increase in $\Delta T$ towards 1 K, the gain declines again.

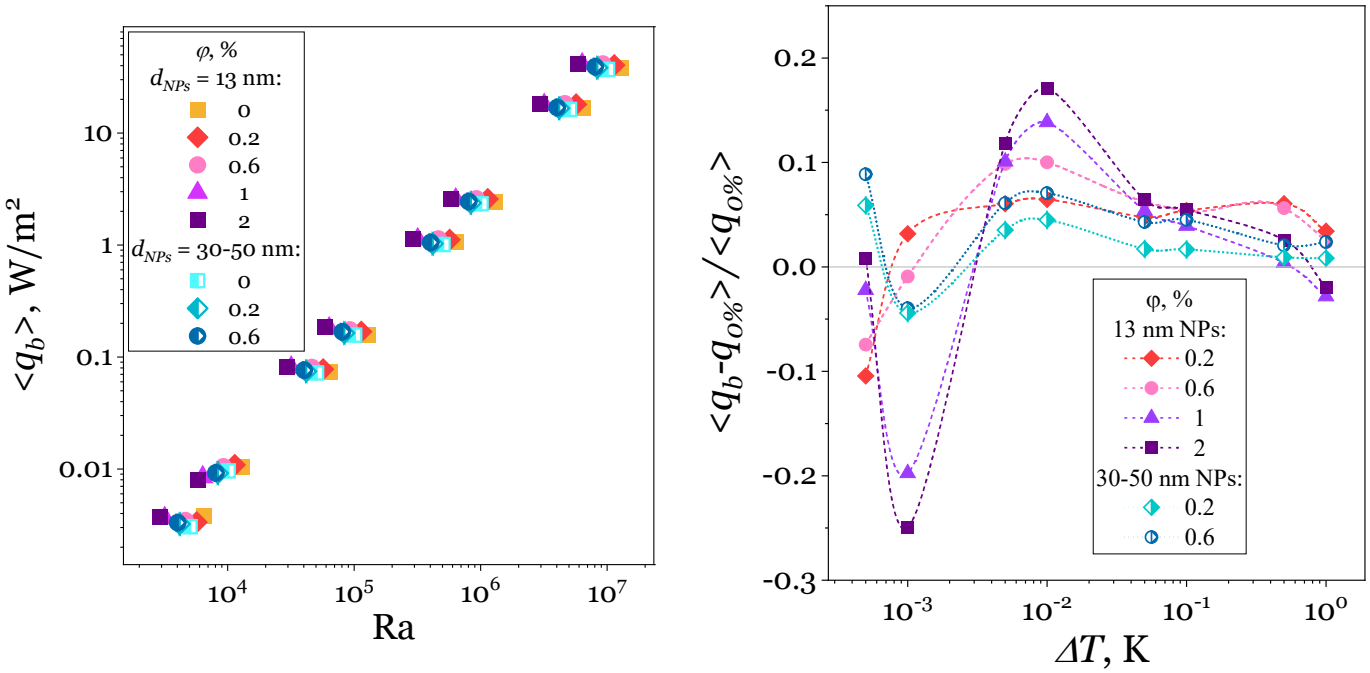


(**a**) (**b**)

**Figure 11.** (**a**) Mean boundary heat flux <$q_b$> dependence on Ra and (**b**) relative change in boundary heat flux compared to pure water <$q_b - q_{0\%}$>/<$q_{0\%}$> dependence on $\Delta T$.

The following factor may be responsible for the observed decrease in the relative heat flux in nanofluids at $\Delta T$ of 0.001 K. As shown in Figure 4, there is a two-fold increase in Pr for nanofluids with $d_{NPs}$ = 13 nm at $\varphi$ = 2%. At a constant $\Delta T$, an increase in Pr enhances the influence of viscosity relative to heat diffusivity, resulting in the increased dissipation of ascending plumes. This dissipation may explain the decrease in convective heat transfer due to viscosity growth. This is also consistent with the slower alteration of convective patterns with $\Delta T$ for higher Pr and $\varphi$, as shown in Figure 9.

As $\Delta T$ increases to 0.05 K, it seems that the higher viscosity of nanofluids does not play as significant a role as it does at $\Delta T$ = 0.001 K, which is consistent with the fact that at $\Delta T$ = 0.05 K, nanofluids and the base fluid show the same patterns (Figure 9). Therefore, the increase in relative heat flux can be attributed to the increased thermal conductivity with higher $\varphi$.

There is no experimental data available that exactly matches the studied range of Ra, the composition of the nanofluid, and the geometry of the fluid domain. However, the closest benchmark is a cubic cell (Ra $\approx 2 \times 10^7$) with $\varphi$ = up to 2%, reporting Nu $\approx$ 20 [47], whereas our model gives Nu $\approx$ 10 at $1 \times 10^7$ (extrapolating to $\lesssim$17 at $2 \times 10^7$). This modest gap likely reflects geometric and experimental differences, although these differences are small.

## 4. Conclusions

This work presents a three-dimensional finite element study of Rayleigh–Bénard convection in $Fe_3O_4/H_2O$ nanofluids containing NPs with two different diameters ($d_{NPs}$ = 13 nm and $d_{NPs}$ = 30–50 nm) at volume fractions up to 2% and within a Rayleigh number range between $10^3$ to $10^7$. The study reveals the influence of NPs volume fraction and particle size on both the flow patterns and heat transfer efficiency.

We constructed flow regime maps that show delayed transitions to more chaotic, higher-intensity convective patterns with an increase in Ra at higher NP volume fractions

$\varphi$. For $d_{NPs}$ = 13 nm, in particular, increasing the volume fraction from 0 to 2% elevates the Prandtl number twice, which indicates the growing role of viscous effects. As a result, the appearance of intricate flow structures (as spiral defect patterns) is shifted to higher Rayleigh numbers compared to pure water. In contrast, larger NPs ($d_{NPs}$ = 30–50 nm) show a milder impact on the base fluid's properties, leading to smaller changes in both the Prandtl number and the convection pattern transitions.

At moderate Rayleigh numbers (Ra $\approx 10^4$), nanofluids with $d_{NPs}$ = 13 nm at $\varphi$ = 2% exhibit up to a 25% reduction in heat flux relative to pure water. This effect may be attributed to the viscosity increase with $\varphi$, which weakens convective motions by dissipating ascending buoyant plumes. This is consistent with the slower transition to the labyrinth pattern with Ra for higher $\varphi$ volume fractions. Conversely, at higher Rayleigh numbers Ra $\gtrsim 10^5$, it is seen that the augmented thermal conductivity begins to play a more dominant role, enabling a net heat flux enhancement of up to 18% compared to pure water at $\varphi$ = 2%.

For larger NPs of $d_{NPs}$ = 30–50 nm, there is a smoother and less pronounced trend in the dependence of the relative heat flux on the Rayleigh number. At Ra $\approx 10^4$, the loss of heat transfer efficiency may amount to around 4% at $\varphi$ = 0.2–0.6%.

From an engineering perspective, this non-monotonic behavior suggests that designers can exploit the tradeoff between viscosity and thermal conductivity to tailor nanofluid applications for specific temperature ranges. These findings can be applied to the development of advanced thermal management systems in electronics and biosciences, where controlled convective heat transfer is essential.

The main limitation of the present work is the use of a single-phase continuum model to describe nanofluid flow. While this approach is widely used [41] and justified at the low particle volume fractions ($\varphi \leq 2\%$), it cannot capture discrete particle–fluid interactions that may become significant for higher $\varphi$.

In order to provide experimental validation of the proposed modelling results, we will construct a convection cell equipped with a particle image velocimetry system for particle tracking and a magnetic lensing system for precise control of magnetic flow. Experimental investigations will be focused on thermogravitational convection in nanofluids containing $Re_xFe_{3-x}O_4$ and TM(Re)ZnO nanoparticles doped with rare-earth elements (Re = Gd, Eu, Dy, Tb, Au, Ag) and transition metals (TM = Mn, Fe, Co, Cu), covering volume fractions $\varphi$ = 0–2% and Ra from $10^3$ up to and beyond $10^7$.

**Author Contributions:** Conceptualization, A.S.F. and M.M.; methodology, A.S.F. and M.M.; software, A.S.F. and M.M.; validation, M.M.; formal analysis, M.M.; investigation, A.S.F. and M.M.; resources, A.S.F.; data curation, A.S.F. and M.M.; writing—original draft preparation, M.M.; writing—review and editing, A.S.F., I.Z. and J.F.; visualization, A.S.F. and M.M.; supervision, A.S.F. All authors have read and agreed to the published version of the manuscript.

**Funding:** This research received no external funding.

**Data Availability Statement:** The raw data supporting the conclusions of this article will be made available by the authors on request.

**Acknowledgments:** The authors acknowledge the ARIADNA Collaboration (Applied Research Infrastructure for Advanced Developments at the NICA facility) and the Joint Institute for Nuclear Research (JINR) for their valuable support in this research.

**Conflicts of Interest:** The authors declare no conflicts of interest.

## Abbreviations

The following abbreviations are used in this manuscript:

| | |
|---|---|
| NP | Nanoparticle |
| MWCNT | Multi-Walled Carbon Nanotube |
| XRD | X-Ray Diffraction |
| LBM | Lattice Boltzmann method |
| EG | Ethylene glycol |
| BDF | Backward differentiation formula |

## References


1. Semenova, E.M.; Vorobyova, S.A.; Lesnikovich, A.I.; Fedotova, J.A.; Bayev, V.G. Fabrication and Investigation of Magnetite Nanoparticles with Gold Shell. *J. Alloys Compd.* **2012**, *530*, 97–101. [CrossRef]
2. Maximenko, A.; Depciuch, J.; Łopuszyńska, N.; Stec, M.; Światkowska-Warkocka, Ż.; Bayev, V.; Zieliński, P.M.; Baran, J.; Fedotova, J.; Węglarz, W.P.; et al. $Fe_3O_4$ @$SiO_2$ @Au Nanoparticles for MRI-Guided Chemo/NIR Photothermal Therapy of Cancer Cells. *RSC Adv.* **2020**, *10*, 26508–26520. [CrossRef] [PubMed]
3. Philip, J. Magnetic Nanofluids (Ferrofluids): Recent Advances, Applications, Challenges, and Future Directions. *Adv. Colloid Interface Sci.* **2023**, *311*, 102810. [CrossRef] [PubMed]
4. Nguyen, M.D.; Tran, H.-V.; Xu, S.; Lee, T.R. $Fe_3O_4$ Nanoparticles: Structures, Synthesis, Magnetic Properties, Surface Functionalization, and Emerging Applications. *Appl. Sci.* **2021**, *11*, 11301. [CrossRef]
5. Pacio, J. 3—Thermal-Hydraulic Experiments with Liquid Metals—Introduction. In *Thermal Hydraulics Aspects of Liquid Metal Cooled Nuclear Reactors*; Roelofs, F., Ed.; Woodhead Publishing: Cambridge, UK, 2019; pp. 45–47, ISBN 978-0-08-101980-1.
6. Li, Y.; Liu, F.; Li, X.; Jin, H. Flow and Heat Transfer Characteristics of Natural Convection in Hydrothermal Reactor with Segmented Heating. *Appl. Therm. Eng.* **2023**, *227*, 120451. [CrossRef]
7. Zhang, L.; Yang, M.; Jiang, M. Mathematical Modeling for Convection-Enhanced Drug Delivery. *Procedia Eng.* **2012**, *29*, 268–274. [CrossRef]
8. Vallejo, J.P.; Prado, J.I.; Lugo, L. Hybrid or Mono Nanofluids for Convective Heat Transfer Applications. A Critical Review of Experimental Research. *Appl. Therm. Eng.* **2022**, *203*, 117926. [CrossRef]
9. Gupta, M.; Singh, V.; Kumar, R.; Said, Z. A Review on Thermophysical Properties of Nanofluids and Heat Transfer Applications. *Renew. Sustain. Energy Rev.* **2017**, *74*, 638–670. [CrossRef]
10. Choi, S.U.S.; Eastman, J. Enhancing Thermal Conductivity of Fluids with Nanoparticles. In Proceedings of the ASME International Mechanical Engineering Congress & Exposition, San Francisco, CA, USA, 12–17 November 1995; Volume 66.
11. Kalsi, S.; Kumar, S.; Kumar, A.; Alam, T.; Dobrotă, D. Thermophysical Properties of Nanofluids and Their Potential Applications in Heat Transfer Enhancement: A Review. *Arab. J. Chem.* **2023**, *16*, 105272. [CrossRef]
12. Faraz, N.; Shemyal Nisar, M.; Khan, Y.; Hussain, A.; Iqbal, K. Natural Convection of Cu-$H_2O$ Nanofluid inside Hexagonal Enclosure Fitted with a Square Cavity with a Non-Uniformly Heated Wall(s). *Results Phys.* **2023**, *51*, 106648. [CrossRef]
13. Liang, Q.; Valizadeh, K.; Bateni, A.; Patra, I.; Abdul-Fattah, M.N.; Kandeel, M.; Zahra, M.M.A.; Bashar, B.S.; Baghaei, S.; Esmaeili, S. The Effect of Type and Size of Nanoparticles and Porosity on the Pool Boiling Heat Transfer of Water/Fe Nanofluid: Molecular Dynamics Approach. *J. Taiwan Inst. Chem. Eng.* **2022**, *136*, 104409. [CrossRef]
14. Li, S.; Zhuo, Z.; He, L.; Huang, X. Atomization Characteristics of Nano-Al/Ethanol Nanofluid Fuel in Electrostatic Field. *Fuel* **2019**, *236*, 811–819. [CrossRef]
15. Chun, S.-Y.; Bang, I.C.; Choo, Y.-J.; Song, C.-H. Heat Transfer Characteristics of Si and SiC Nanofluids during a Rapid Quenching and Nanoparticles Deposition Effects. *Int. J. Heat Mass Transf.* **2011**, *54*, 1217–1223. [CrossRef]
16. Hemmat Esfe, M.; Alidoust, S.; Toghraie, D. Comparison of Thermal Conductivity of Water-Based Nanofluids with Various Combinations of MWCNT, CuO, and $SiO_2$ Nanoparticles for Using in Heating Systems. *Case Stud. Therm. Eng.* **2023**, *42*, 102683. [CrossRef]
17. Kumar, N.; Sonawane, S.S. Experimental Study of $Fe_2O_3$/Water and $Fe_2O_3$/Ethylene Glycol Nanofluid Heat Transfer Enhancement in a Shell and Tube Heat Exchanger. *Int. Commun. Heat Mass Transf.* **2016**, *78*, 277–284. [CrossRef]
18. Liu, Z.; Wang, X.; Gao, H.; Yan, Y. Experimental Study of Viscosity and Thermal Conductivity of Water Based $Fe_3O_4$ Nanofluid with Highly Disaggregated Particles. *Case Stud. Therm. Eng.* **2022**, *35*, 102160. [CrossRef]
19. Ajeeb, W.; Thieleke da Silva, R.R.S.; Murshed, S.M.S. Experimental Investigation of Heat Transfer Performance of $Al_2O_3$ Nanofluids in a Compact Plate Heat Exchanger. *Appl. Therm. Eng.* **2023**, *218*, 119321. [CrossRef]

20. Almanassra, I.W.; Manasrah, A.D.; Al-Mubaiyedh, U.A.; Al-Ansari, T.; Malaibari, Z.O.; Atieh, M.A. An Experimental Study on Stability and Thermal Conductivity of Water/CNTs Nanofluids Using Different Surfactants: A Comparison Study. *J. Mol. Liq.* **2020**, *304*, 111025. [CrossRef]
21. Lin, H.; Jian, Q.; Bai, X.; Li, D.; Huang, Z.; Huang, W.; Feng, S.; Cheng, Z. Recent Advances in Thermal Conductivity and Thermal Applications of Graphene and Its Derivatives Nanofluids. *Appl. Therm. Eng.* **2023**, *218*, 119176. [CrossRef]
22. Aswarthanarayana, S.; Rajan, A.; Raj, R.; Ranjan, G.; Prasad, L. Investigation of Thermal Properties of Graphene-Silicone Oil Nanofluid. *Mater. Today Proc.* **2023**, *76*, 376–382. [CrossRef]
23. Fan, W.; Zhong, F. Experimental Study on Thermal Conductivity of Kerosene-Based Nanofluids. *Thermochim. Acta* **2022**, *712*, 179229. [CrossRef]
24. Arafat, R.; Köhn, C.; Jean-Fulcrand, A.; Abraham, T.; Garnweitner, G.; Herrmann, C. Physical-Chemical Properties and Tribological Characterization of Water-Glycerine Based Metal Oxide Nanofluids. *J. Mater. Res. Technol.* **2023**, *25*, 2112–2126. [CrossRef]
25. Bao, L.; Zhong, C.; Jie, P.; Hou, Y. The Effect of Nanoparticle Size and Nanoparticle Aggregation on the Flow Characteristics of Nanofluids by Molecular Dynamics Simulation. *Adv. Mech. Eng.* **2019**. [CrossRef]
26. Wei, Y.; Han, B.; Hu, X.; Lin, Y.; Wang, X.; Deng, X. Synthesis of $Fe_3O_4$ Nanoparticles and Their Magnetic Properties. *Procedia Eng.* **2012**, *27*, 632–637. [CrossRef]
27. Rajan, A.; Sharma, M.; Sahu, N.K. Assessing Magnetic and Inductive Thermal Properties of Various Surfactants Functionalised $Fe_3O_4$ Nanoparticles for Hyperthermia. *Sci. Rep.* **2020**, *10*, 15045. [CrossRef]
28. Santoyo Salazar, J.; Perez, L.; de Abril, O.; Truong Phuoc, L.; Ihiawakrim, D.; Vazquez, M.; Greneche, J.-M.; Begin-Colin, S.; Pourroy, G. Magnetic Iron Oxide Nanoparticles in 10−40 Nm Range: Composition in Terms of Magnetite/Maghemite Ratio and Effect on the Magnetic Properties. *Chem. Mater.* **2011**, *23*, 1379–1386. [CrossRef]
29. Jang, S.P.; Choi, S.U.S. Free Convection in a Rectangular Cavity (Benard Convection) with Nanofluids. In Proceedings of the ASME 2004 International Mechanical Engineering Congress and Exposition, Anaheim, CA, USA, 13–19 November 2004; Volume 3, pp. 147–153.
30. Putra, N.; Roetzel, W.; Das, S.K. Natural Convection of Nano-Fluids. *Heat Mass Transf.* **2003**, *39*, 775–784. [CrossRef]
31. Ruo, A.-C.; Yan, W.-M.; Chang, M.-H. The Onset of Natural Convection in a Horizontal Nanofluid Layer Heated from Below. *Heat Transf.* **2021**, *50*, 7764–7783. [CrossRef]
32. Sheikholeslami, M. Magnetic Source Impact on Nanofluid Heat Transfer Using CVFEM. *Neural Comput. Appl.* **2018**, *30*, 1055–1064. [CrossRef]
33. Sheikholeslami, M.; Ellahi, R.; Vafai, K. Study of $Fe_3O_4$-Water Nanofluid with Convective Heat Transfer in the Presence of Magnetic Source. *Alex. Eng. J.* **2018**, *57*, 565–575. [CrossRef]
34. Feng, Y.; Wang, C. Lattice Boltzmann Study on Magnetohydrodynamic Double-Diffusive Convection in $Fe_3O_4$–$H_2O$ Nanofluid-Filled Porous Media. *Case Stud. Therm. Eng.* **2024**, *58*, 104405. [CrossRef]
35. Weng, L.; Rahmani, A.; Mohammad Sajadi, S.; Kumar, A.; Ulloa, N.; Firas Abdulameer, S.; Alawadi, A.; Alsalamy, A.; Salahshour, S.; Zarringhalam, M.; et al. Simulation of Natural Convection of Nanofluid inside a Square Cavity Using Experimental Data by Lattice Boltzmann Method. *Ain Shams Eng. J.* **2024**, *15*, 102711. [CrossRef]
36. Li, L.; Xu, P.; Li, Q.; Zheng, R.; Xu, X.; Wu, J.; He, B.; Bao, J.; Tan, D. A Coupled LBM-LES-DEM Particle Flow Modeling for Microfluidic Chip and Ultrasonic-Based Particle Aggregation Control Method. *Appl. Math. Model.* **2025**, *143*, 116025. [CrossRef]
37. Li, L.; Xu, P.; Li, Q.; Yin, Z.; Zheng, R.; Wu, J.; Bao, J.; Bai, W.; Qi, H.; Tan, D. Multi-Field Coupling Particle Flow Dynamic Behaviors of the Microreactor and Ultrasonic Control Method. *Powder Technol.* **2025**, *454*, 120731. [CrossRef]
38. Tan, Y.; Ni, Y.; Xu, W.; Xie, Y.; Li, L.; Tan, D. Key Technologies and Development Trends of the Soft Abrasive Flow Finishing Method. *J. Zhejiang Univ. -Sci. A* **2023**, *24*, 1043–1064. [CrossRef]
39. Xu, P.; Li, Q.; Wang, C.; Li, L.; Tan, D.; Wu, H. Interlayer Healing Mechanism of Multipath Deposition 3D Printing Models and Interlayer Strength Regulation Method. *J. Manuf. Process.* **2025**, *141*, 1031–1047. [CrossRef]
40. Chen, H.; Zhang, H.; Thi, N.H.; Afrand, M. A Review on the Role of Molecular Dynamics in Discovering Behaviors, Heat Transfer, and Properties of Nanofluids. *J. Mol. Liq.* **2024**, *415*, 126238. [CrossRef]
41. Alsabery, A.I.; Abosinnee, A.S.; Al-Hadraawy, S.K.; Ismael, M.A.; Fteiti, M.A.; Hashim, I.; Sheremet, M.; Ghalambaz, M.; Chamkha, A.J. Convection Heat Transfer in Enclosures with Inner Bodies: A Review on Single and Two-Phase Nanofluid Models. *Renew. Sustain. Energy Rev.* **2023**, *183*, 113424. [CrossRef]
42. Khanafer, K.; Vafai, K.; Lightstone, M. Buoyancy-Driven Heat Transfer Enhancement in a Two-Dimensional Enclosure Utilizing Nanofluids. *Int. J. Heat Mass Transf.* **2003**, *46*, 3639–3653. [CrossRef]
43. Roy, N.C. Natural Convection of Nanofluids in a Square Enclosure with Different Shapes of Inner Geometry. *Phys. Fluids* **2018**, *30*, 113605. [CrossRef]
44. Nnanna, A.G.A.; Fistrovich, T.; Malinski, K.; Choi, S.U.S. Thermal Transport Phenomena in Buoyancy-Driven Nanofluids. In Proceedings of the ASME 2004 International Mechanical Engineering Congress and Exposition, Anaheim, CA, USA, 13–19 November 2004; pp. 571–578.

45. Joshi, P.S.; Pattamatta, A. Buoyancy Induced Convective Heat Transfer in Particle, Tubular and Flake Type of Nanoparticle Suspensions. *Int. J. Therm. Sci.* **2017**, *122*, 1–11. [CrossRef]
46. Pazarlioğlu, H.K.; TekiR, M. Impact of $Fe_3O_4$/Water on Natural Convection in Square Enclosure. *Eur. J. Sci. Technol.* **2021**, 675–683. [CrossRef]
47. Kamran, M.; Qayoum, A. Experimental Investigation of Natural Convection of $Fe_3O_4$-Water Nanofluid in a Cubic Cavity. *J. Dispers. Sci. Technol.* **2024**, *45*, 651–661. [CrossRef]
48. Alami, A.H.; Ramadan, M.; Tawalbeh, M.; Haridy, S.; Al Abdulla, S.; Aljaghoub, H.; Ayoub, M.; Alashkar, A.; Abdelkareem, M.A.; Olabi, A.G. A Critical Insight on Nanofluids for Heat Transfer Enhancement. *Sci. Rep.* **2023**, *13*, 15303. [CrossRef]
49. Pandey, A.; Scheel, J.D.; Schumacher, J. Turbulent Superstructures in Rayleigh-Bénard Convection. *Nat. Commun.* **2018**, *9*, 2118. [CrossRef]
50. Pesch, W. Complex Spatiotemporal Convection Patterns. *Chaos Interdiscip. J. Nonlinear Sci.* **1996**, *6*, 348–357. [CrossRef]
51. Dillon, H.E. Dimensionless versus Dimensional Analysis in CFD and Heat Transfer. In Proceedings of the COMSOL Conference, Boston, MA, USA, 7–9 October 2010.
52. Schumacher, J.; Bandaru, V.; Pandey, A.; Scheel, J.D. Transitional Boundary Layers in Low-Prandtl-Number Convection. *Phys. Rev. Fluids* **2016**, *1*, 084402. [CrossRef]
53. Zhang, Y.; Zhou, Q.; Sun, C. Statistics of Kinetic and Thermal Energy Dissipation Rates in Two-Dimensional Turbulent Rayleigh–Bénard Convection. *J. Fluid Mech.* **2017**, *814*, 165–184. [CrossRef]
54. Wang, B.; Zhou, Q.; Sun, C. Vibration-Induced Boundary-Layer Destabilization Achieves Massive Heat-Transport Enhancement. *Sci. Adv.* **2020**, *6*, eaaz8239. [CrossRef]
55. Guermond, J.L.; Minev, P.; Shen, J. An Overview of Projection Methods for Incompressible Flows. *Comput. Methods Appl. Mech. Eng.* **2006**, *195*, 6011–6045. [CrossRef]
56. Pallares, J.; Cuesta, I.; Grau, F.X. Laminar and Turbulent Rayleigh–Bénard Convection in a Perfectly Conducting Cubical Cavity. *Int. J. Heat Fluid Flow* **2002**, *23*, 346–358. [CrossRef]
57. Syam Sundar, L.; Singh, M.K.; Sousa, A.C.M. Investigation of Thermal Conductivity and Viscosity of $Fe_3O_4$ Nanofluid for Heat Transfer Applications. *Int. Commun. Heat Mass Transf.* **2013**, *44*, 7–14. [CrossRef]
58. Pak, B.C.; Cho, Y.I. Hydrodynamic and Heat Transfer Study of Dispersed Fluids with Submicron Metallic Oxide Particles. *Exp. Heat Transf.* **1998**, *11*, 151–170. [CrossRef]
59. Krakov, M.S.; Zakinyan, A.R.; Zakinyan, A.A. Instability of the Miscible Magnetic/Non-Magnetic Fluid Interface. *J. Fluid Mech.* **2021**, *913*, A30. [CrossRef]
60. Li, X.-M.; He, J.-D.; Tian, Y.; Hao, P.; Huang, S.-D. Effects of Prandtl Number in Quasi-Two-Dimensional Rayleigh–Bénard Convection. *J. Fluid Mech.* **2021**, *915*, A60. [CrossRef]
61. Assenheimer, M.; Steinberg, V. Critical Phenomena in Hydrodynamics. *Europhys. News* **1996**, *27*, 143–147. [CrossRef]
62. Xi, H.; Gunton, J.D.; Viñals, J. Spiral Defect Chaos in a Model of Rayleigh-Bénard Convection. *Phys. Rev. Lett.* **1993**, *71*, 2030–2033. [CrossRef]
63. Fonda, E.; Pandey, A.; Schumacher, J.; Sreenivasan, K.R. Deep Learning in Turbulent Convection Networks. *Proc. Natl. Acad. Sci. USA* **2019**, *116*, 8667–8672. [CrossRef]